Solid-state dewetting mechanisms of ultrathin Ni films revealed by combining *in situ* time resolved differential reflectometry monitoring and atomic force microscopy

Erik J. Luber, Brian C. Olsen, Colin Ophus, and David Mitlin
Department of Chemical and Materials Engineering, University of Alberta, Edmonton, Alberta, Canada and National Institute for Nanotechnology, Edmonton, Alberta, Canada
(Received 20 April 2010; revised manuscript received 2 July 2010; published 4 August 2010)

In this study we report on the solid-state dewetting of ultrathin Ni films on amorphous SiO_2. The dewetting process is monitored *in situ* using time resolved differential reflectometry (TRDR). The time resolved differential reflectivity signal during dewetting is found to exhibit a rich behavior, which is intimately connected the changes in morphology. Finite-difference time-domain simulation is used to explain the observed reflectivity data, where experimentally acquired atomic force microscope heightmaps are used as simulation inputs. From *ex situ* atomic force microscope heightmaps, the sequential processes of grain growth, grain boundary grooving, hole growth, and particle coarsening are observed. Grain growth of ultrathin films prior to dewetting is critically important in determining the particle density, which has been largely unexplored in previous dewetting studies. Kinetic analysis of the TRDR data revealed two rate-limiting processes, with activation energies of 0.31 ± 0.04 and 0.59 ± 0.06 eV. We hypothesize that these kinetic pathways correspond to Ni grain growth and surface mass self-diffusion on the Ni(111) planes, respectively.

DOI: 10.1103/PhysRevB.82.085407 PACS number(s): 78.67.Bf, 78.47.jg, 68.37.Ps, 68.60.Dv

I. INTRODUCTION

Many technologically important thin film/substrate systems are found to be unstable at temperatures well below their melting point, where the thin film breaks up into small islands.[1–6] This instability is know as dewetting or agglomeration, which is a result of minimizing the total system energy driven by differences in surface free energies of the film surface and the film/substrate interface.

Dewetting is a serious concern in microelectronics reliability as it is intimately linked to copper interconnect reliability.[7–9] Conversely, many applications utilize nanoparticles and nanoholes, which can be produced via solid-state dewetting, such as the fabrication of optoelectronic devices,[10] subwavelength resonance focusing,[11] and catalysis.[12,13] As such, a fundamental and quantitative understanding of the mechanisms governing solid-state dewetting is of particular relevance.

Theoretically the final morphology of the dewet state is governed by the so-called Rayleigh instability,[14,15] which leads to a characteristic particle spacing. However, the Rayleigh instability is rarely observed since the dewetting of polycrystalline films is strongly influenced by the presence of grain boundaries and grain-boundary triple junctions.[16] As identified by Mullins[17] in 1957, thermal grooving is the origin of dewetting in the presence of grain boundaries. Using continuum methods, the stability of a periodic arrangement of identical grains was analyzed by Srolovitz and Safran[18] in 1986, this was expanded upon by Rha and Park[19] in 1997. Recently, Pierre-Louis *et al.*[20] have employed kinetic Monte Carlo simulations to elucidate the important role of faceting during dewetting. However, a firm theoretical understanding of solid-state dewetting has been slow due to the complex and varied nature of a real arrangement of grains composing a film.

In recent years a few authors have made use of *in situ* and realtime techniques, which have expanded our understanding solid-state dewetting. The van der Pauw method has been used to monitor realtime changes in electrical resistance of Cu films on SiO_2 during *ex situ* heating.[4] Other authors have performed *in situ* electrical monitoring of dewetting Ni films.[21] Electrical monitoring provides quantitative kinetic information, however, it cannot probe the significant morphological changes that occur beyond the percolation limit (electrical breakdown). Moreover, to avoid compositional changes during *in situ* four-point probe resistance measurements, the voltage and current leads must fabricated from the same material as the film under investigation,[21] which severely limits the class of materials that can be investigated in this way. Alternatively, *in situ* grazing incidence small-angle x-ray scattering (GISAXS) has been utilized to probe morphological changes that occur during dewetting[1,22] of Ni films. However, even when using synchrotron-radiation GISAXS is only quasirealtime with acquisition times on the order of ~40 s. Another limitation is the size of particles that can be studied[23] and does not provide quantitative kinetic information. Moreover, a complete morphological interpretation is fundamentally limited to model-based inversion.

In this study we utilized *in situ* time resolved differential reflectometry (TRDR) coupled with atomic force microscopy (AFM) to investigate dewetting kinetics and morphological changes in Ni films on amorphous SiO_2. Dewetting of Ni films on SiO_2 is important for new flash memory technologies,[24] growth of carbon nanotubes,[12,13,25] and potential nanomagnetic properties.[26] TRDR is simple to implement, nondestructive, and can be used to probe dewetting of virtually any sample type. From these measurements we identify four sequential stages of dewetting Ni films on SiO_2 and measure activation energies of two kinetically limiting processes. Moreover, the observed optical response is understood via three-dimensional finite-difference time-domain (FDTD) simulation, using acquired AFM height maps as simulation inputs.

 ©2010 The American Physical Society

II. METHODS

A. Experimental

The substrates used in this study were (100) oriented silicon wafers that were thermally oxidized in a wet environment using a custom built furnace (Tystar Inc.). Prior to oxidation, the Si wafers were cleaned using a 3:1 mixture of $H_2SO_4:H_2O_2$. The thickness of the oxide layer was measured using a F50 spectral reflectance automated thickness mapper (Filmetrics Inc.) and subsequently cleaved into 1 cm × 1 cm chips, keeping only chips having SiO_2 thicknesses within ±1 nm of each other. These chips were stored in a vacuum chamber at base pressures of $\sim 1 \times 10^{-7}$ Torr.

Ni films with thicknesses between 2.0 and 9.0 nm were deposited at a constant rate of 0.62 Å/s using a dc magnetron sputtering system (AJA International) at UHV conditions (base pressure $< 9 \times 10^{-10}$ Torr). Argon sputtering was maintained at 4 mTorr and 100 W. Deposition rates were determined using a quartz crystal deposition monitor. Interfacial mixing during deposition is expected to negligible during deposition. As shown by Qiu *et al.*,[27] using both reflection high-energy electron diffraction and transmission electron microscopy, there is no interfacial mixing that occurs during dc magnetron sputtering of Ni on SiO_2. Moreover, the equilibrium phase diagram shows that Ni and SiO_2 have negligible mutual solubility at all temperatures considered in this study.

Prior to deposition each chip was annealed in the UHV chamber at 500 °C for 2 h and allowed to cool for >12 hours. Following deposition the films were vacuum heated at the desired ramp rate to 500 °C and held for 2 h at this temperature. The temperature was measured using a thermocouple and was estimated to have an error of less than ±5 °C at temperatures above 150 °C.

During all stages of UHV chip processing (predeposition anneal, deposition, and postdeposition heating) the optical reflectivity was monitored. TRDR is performed using a 660 nm *s*-polarized AlGaInP diode laser operating at 16 mW. The beam is incident upon the films 30° from the substrate normal. The specular beam intensity was measured using a ILT 1700 light meter (International Light Technology) using a silicon detector. The incident and reflected beam traveled through the vacuum chamber via transparent silica windows. The parameter of interest is the change in reflectivity R, with respect to the initial substrate reflectivity R_0 prior to deposition

$$\frac{\Delta R}{R} = \frac{R - R_0}{R_0}. \quad (1)$$

The film morphologies were analyzed using a multimode AFM (Veeco Instruments Inc.) operating in tapping mode. Films having large features were scanned with ACTA tips (AppNano) having a nominal tip radius of 6 nm using a *E*-type piezo element which allowed for 10 μm of horizontal scanning. Films having smaller features were scanned with ACTA-SS tips (AppNano) having a nominal tip radius of 2 nm using a *A*-type piezo element which allowed for 1 μm of horizontal scanning.

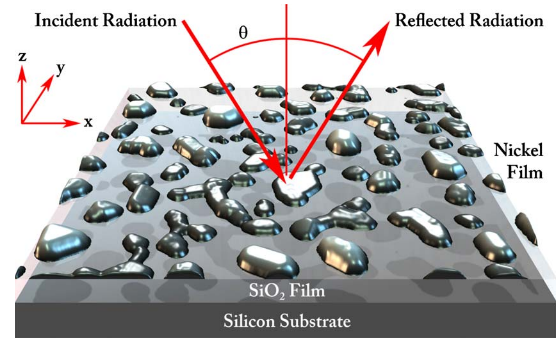

FIG. 1. (Color online) Geometry used for FDTD calculations of dewet Ni films on SiO_2.

Film texture was analyzed using x-ray diffraction (XRD), which was performed using a Bruker AXS D8 general area detector diffraction system. A Cu Kα radiation source (λ = 1.54056 Å) collected the x-ray scans from a sample mounted on a two-axis rotation stage that also allowed for *XYZ* translation.

B. Simulation

The optical changes in the films that occur during dewetting were analyzed using FDTD simulation. The FDTD calculations were performed using commercially available software from Lumerical Solutions Inc. For all simulations, experimentally acquired AFM heightmaps were used as inputs to correctly represent the morphology of the films. Shown in Fig. 1 is a representative schematic of the simulation geometry. Bloch boundary conditions were used in the x and y directions while perfectly matched layer was used in the z direction. A nonuniform mesh was used in z, whose spacing was determined by the index of the material. A uniform mesh spacing was used in the x and y directions, which was set to the resolution of the AFM heightmap (all AFM height maps were acquired at a resolution of 512 × 512 pixels^2, therefore the grid spacing used for a 2 × 2 μm^2 simulation volume was 3.9 nm). Within the Ni layer, a much finer mesh spacing of 0.25 nm was used in the z direction.

Broadband simulations were performed at normal incidence using a planewave source having a spectral range of 400–1400 nm. Dispersion within the Ni was modeled using an eighth order polynomial fit to the experimentally determined dielectric constants in the Lumerical database. Simulations at a non-normal incidence of $\theta = 30°$ were performed using a monochromatic *s*-polarized planewave source at 660 nm. Simulations were stopped when the electrical field dropped below a critical cutoff within the simulation volume.

III. TRDR CHARACTERIZATION OF DEWETTING

Figure 2 shows the TRDR response of Ni films (initial thicknesses ranging from 2.0 to 9.0 nm) on 124 nm of SiO_2, heated from room temperature to 500 °C at 5 °C/min, which was then held at 500 °C for 2 h. We see that the TRDR response exhibits a rich behavior, showing significant

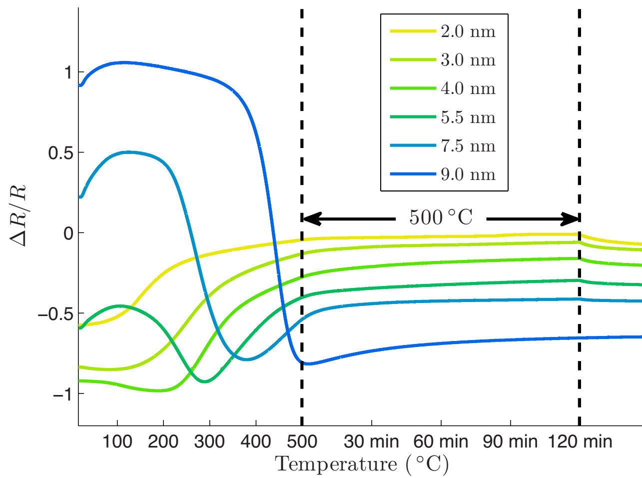

FIG. 2. (Color online) TRDR response of Ni films (initial thicknesses ranging from 2 to 9 nm) on 365 nm of SiO_2, ramped at 5 °C/min, which is then held at 500 °C for 2 h.

variation in both temperature (time) and initial film thickness. Importantly, all films within this thickness range exhibit a minimum in reflectivity (aside from the thinnest film of 2.0 nm). Given that the variation in TRDR response is intimately tied to changes in the Ni film, a detailed investigation of the relation between TRDR response and morphology was performed.

The TRDR signal during the deposition of a 7.0 nm thick Ni film on 365 nm of SiO_2 is shown in Fig. 3(a). Also shown is the theoretical TRDR signal, calculated using the characteristic matrix approach,[28] which assumes the Ni layer is perfectly flat, uniform and utilizes bulk Ni optical constants. Both curves have the same characteristic behavior where the initial addition of a the metal layer results in a *decrease* in reflectivity. However, the minimum reflectivity is experimentally determined to be at 4.0 nm of Ni whereas the characteristic matrix method predicts the minimum reflectivity to occur at a thickness of 1.9 nm. This important discrepancy is a result of the well established fact that inhomogeneities in the film (grain boundaries, voids, etc.) significantly affect optical properties in the visible-UV range.[29]

The initial decrease in the TRDR signal during deposition illustrates the significance of a changing interference condition as the properties of the Ni film change. Simple two-beam interference is a useful conceptual tool for understanding many of the observed optical changes. Prior to the deposition of Ni, the SiO_2/Si stack is near a destructive interference condition for incident radiation at 660 nm and $\theta = 30°$, due to a half integer path-length difference between the primary and secondary reflected beams. However, the amplitude of the primary beam is small in comparison to the secondary beam due to the low reflectivity of the vacuum/SiO_2 interface. The deposition of the Ni layer results in both an increase in the amplitude of the primary beam and a decrease in the amplitude of the secondary beam. As the amplitudes of the primary and secondary beams approach each other the destructive interference becomes more complete, which is the physical origin of the TRDR signal observed during deposition. This situation is much more complex during dewetting, nonetheless a changing interference condition due to changes in the Ni film topography is expected to significantly affect the TRDR signal.

Shown in Fig. 3(b) is the TRDR signal of a 7.0 nm Ni film during heating. The points labeled S1–S7 indicate separate films that were prepared under identical conditions which were heated to the shown temperature then cooled back to room temperature. The respective AFM micrographs are shown in Fig. 4. After an initial increase in reflectivity (this will be discussed in more detail later) there is a rapid and significant decrease in reflectivity. Inspection of micrographs S3–S4 reveal that this decrease in reflectivity is associated with the nucleation and growth of holes in the Ni film, exposing the bare SiO_2 interface. Eventually the reflectivity reaches a minimum, when the film is near the percolation limit (sample S5), followed by a much slower increase in reflectivity, where the film is completely broken up and consists entirely in isolated Ni particles (micrograph S7).

The most common methods used to interpret electromagnetic reflection data of discontinuous metal films are

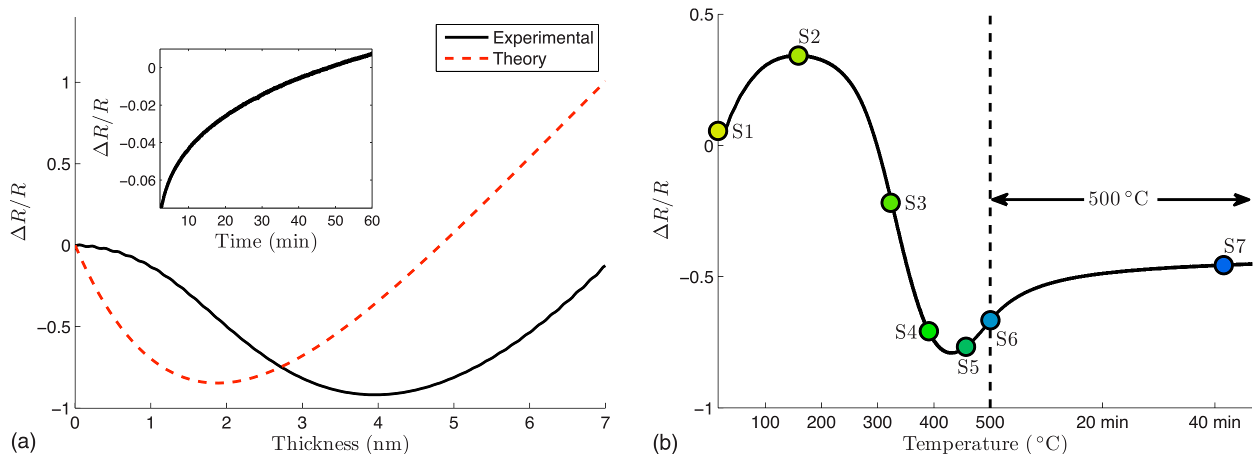

FIG. 3. (Color online) (a) Experimental and theoretical TRDR signals during the deposition of a 7.0 nm thick Ni film on 365 nm of SiO_2. Inset is the change in reflectivity after the deposition is stopped. (b) TRDR signal of a 7.0 nm film during heating at 10 °C/min. Points labeled S1–S7 indicate separate films that were prepared under identical conditions which were heated to the shown temperature then cooled back to room temperature. The respective AFM micrographs are shown in Fig. 4.

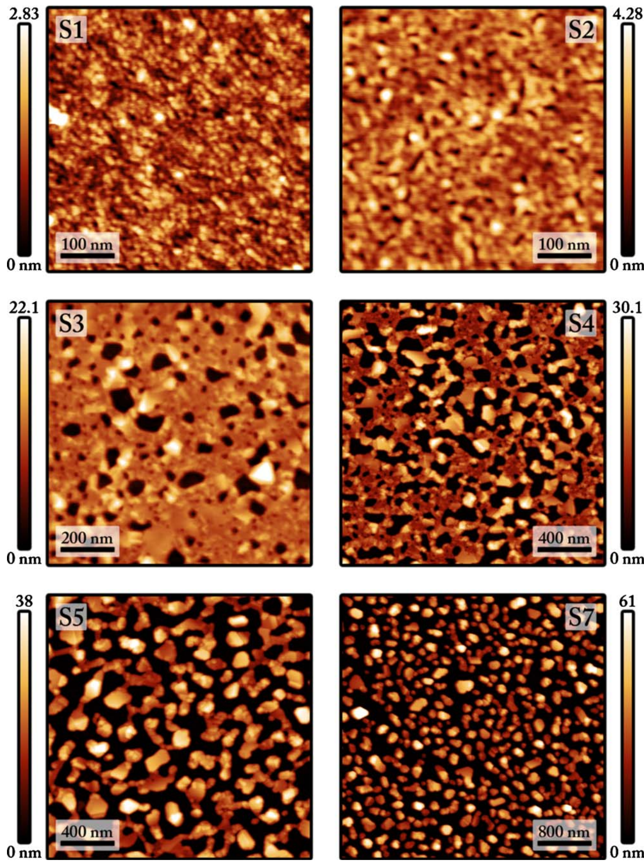

FIG. 4. (Color online) *Ex situ* AFM micrographs of a 7.0 nm thick Ni film during different stages of dewetting. The corresponding film temperature and reflectivity are shown in Fig. 3(b).

effective-medium theories, such as the Maxwell-Garnett and Lorentz-Lorenz theories.[30] However, these methods are limited by the validity of the assumptions used and simplified geometry.[31] Importantly, these theories are not strictly valid near the percolation limit, nor do they provide significant physical insight beyond extracting some mean physical parameters within the framework of the theory. Therefore, to gain a more detailed understanding of the TRDR response during all stages of dewetting, FDTD simulations were performed. The experimentally measured AFM heightmaps of samples S3–S7 were utilized to directly set the film geometry in the simulation.

FDTD Simulation

In order to investigate transmission through a dewetting Ni layer, FDTD simulations of Ni films on a SiO_2 substrate were performed. Inset in Fig. 5(a) is the calculated spectral transmission at normal incidence of samples S3–S7. As expected, transmission through the Ni layer increases as the dewetting process proceeds since more of the SiO_2 surface is being exposed to vacuum. However, the increase in transmission is much greater in the near infrared than the visible portion of the spectrum. This indicates that the change in transmission is not simply in proportion to the area fraction of uncovered substrate.

When studying transmission through optically thick metal hole arrays, it is useful to normalize the transmission spectrum such that it can be interpreted as the effective transmission of the holes in the array.[32] The normalized transmission or transmissivity η, is given by

$$\eta = \frac{T}{QT_{\text{sub}}}, \tag{2}$$

where T is the measured transmission, Q is the area fraction of uncovered substrate, and T_{sub} is the transmittance of the substrate. Using this normalization scheme, a transmissivity greater than unity indicates some extraordinary transmission while a transmissivity less than unity indicates some energy loss as the radiation interacts with the aperture(s). However, we must generalize this definition due to the complication that the films used in this study are on the order of the skin depth, resulting in nonzero transmission through the Ni. The transmissivity is then redefined in the following manner:

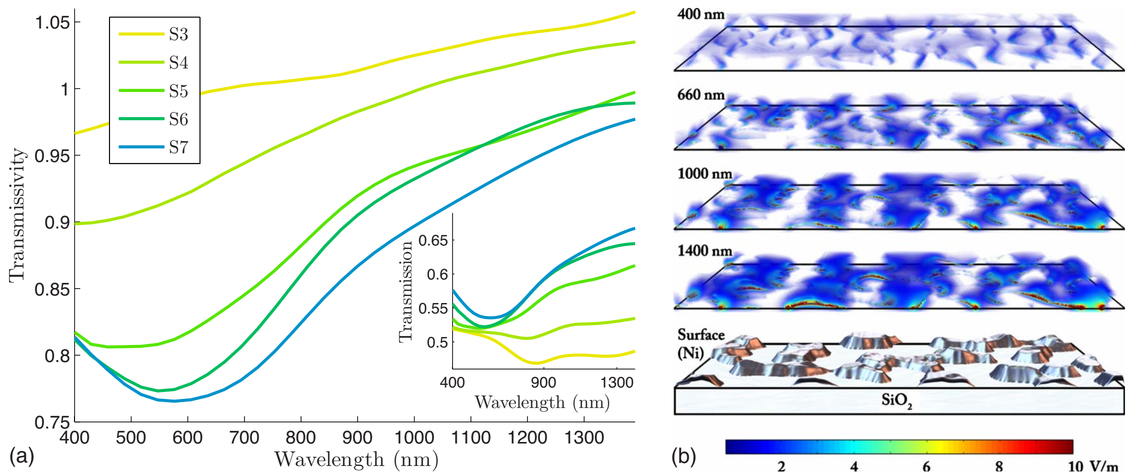

FIG. 5. (Color online) (a) FDTD calculation of the normalized spectral transmissivity (inset: un-normalized transmission) at normal incidence of samples S3–S7 on SiO_2 substrate during different stages of dewetting. (b) Steady-state electric field intensity in a 1 μm $\times 1$ μm region of sample S5 at incident wavelengths of 400, 660, 1000, and 1400 nm.

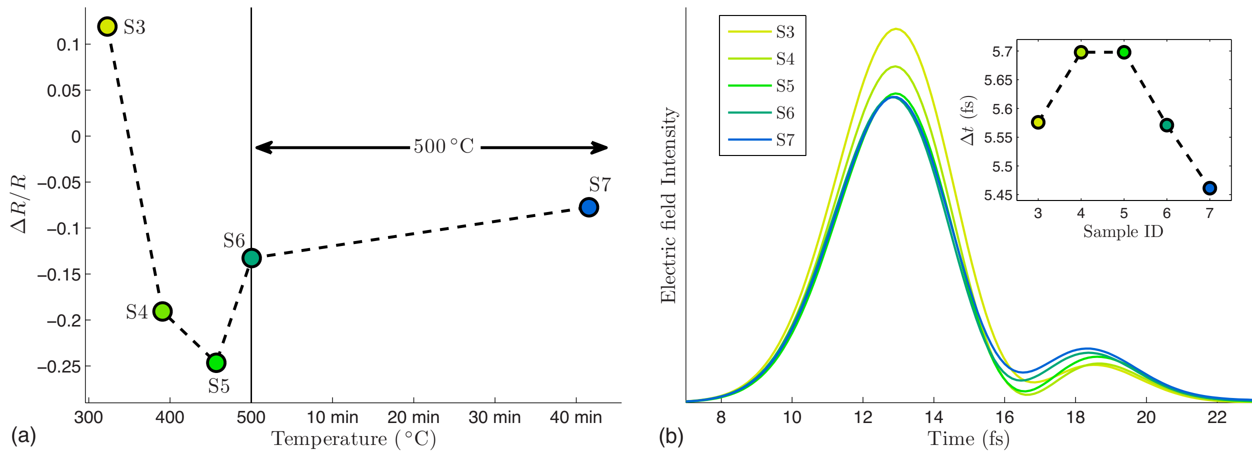

FIG. 6. (Color online) (a) FDTD simulation of TRDR signal during dewetting of 7 nm Ni film on 365 nm SiO_2 having a Si substrate with radiation of 660 nm incident at 30°. The simulations are performed using AFM heightmaps S3–S7. (b) Temporal evolution of the average electric field intensity in a plane above the Ni surface. Inset is the time delay between the peak amplitudes of the primary and secondary pulses.

$$\eta(\lambda) = \frac{T(\lambda)}{\frac{1}{N}\sum_{i=1}^{N} T_i(\lambda)}, \quad (3)$$

where the average is taken over the field of illumination, divided into N locally homogeneous subdomains. The transmission of each subdomain is T_i, which is calculated using the characteristic matrix approach. We see that this definition reduces to Eq. (2) when the transmission through the metal layer is zero.

The transmissivity of samples S3–S7 are shown in Fig. 5(a). We see that transmissivity is generally increasing with wavelength for all samples, with S3 and S4 exhibiting transmissivities greater than unity. Enhanced transmission of subwavelength uncorrelated-random hole arrays has been observed for several different metals,[32] where the enhanced transmission was attributed to so-called site resonances or localized surface-plasmon resonance. More recently, detailed investigation on the role of site resonances in enhanced transmission for wavelength scale square holes has been investigated both theoretically[33] and experimentally.[34] It was found that the enhanced transmission was both spectrally broad and weak with the peak transmission occurring at a wavelength roughly double the hole size.

Site resonances are a consequence of the oscillating radiation producing a force on the mobile electrons in the conduction band, the result of which is to induce a dipole moment in the particle/hole. Figure 5(b) shows the steady-state electric filed intensity in a 1 μm$\times$1 μm region of sample S5 at incident wavelengths of 400, 660, 1000, and 1400 nm. We see the associated induced dipole fields at the edges of the particles due to site resonances, which become more intense at longer wavelengths. The observed increase in transmissivity with wavelength is a consequence of these increasingly intense site resonances. Moreover, the decrease in transmissivity as dewetting proceeds is likely a result of scattering from the wavelength scale particles/holes.[35]

From these simulations we see that the total transmission increases significantly as dewetting proceeds. Investigation of the steady-state electric field shows the presence of site resonances, however, their contribution to transmission is small since the transmissivity is never much greater than unity. This is consistent with the transmission spectra of uncorrelated-random hole arrays.[34] Therefore, we find that the changes in transmission during dewetting are largely driven by ordinary transmission through the oxide and subskin depth Ni, and scattering from the Ni particles/holes.

From the above results it is not entirely clear why the TRDR signal exhibits a minima during dewetting, as seen in Fig. 3(b). The FDTD simulations show that the transmission increases monotonically as dewetting proceeds; therefore, from the perspective of two-beam interference it is expected that the reflectivity decrease monotonically since the initial amplitude of primary beam is larger than the secondary and as dewetting proceeds these amplitudes approach each other. To understand this observed behavior we performed FDTD simulations of samples S3–S7 replicating the experimental configuration (365 nm SiO_2 on a Si substrate with radiation of 660 nm incident at 30°).

The simulated TRDR signal is shown in Fig. 6(a). It agrees well with experiment, having the same characteristic behavior. However, it should be noted that the absolute values of reflectivity are different from that in experiment, which is likely a consequence of the difference in dielectric constants between thin film and bulk.[29] Nonetheless, this result demonstrates that the shape of the TRDR curve can be understood within the set of assumptions used in the FDTD simulations. Shown in Fig. 6(b) is the temporal evolution of the average electric field intensity in a plane above the Ni surface, corresponding to the simulations in Fig. 6(a). This clearly shows both the primary pulse reflected from the vacuum/Ni interface and the secondary pulse reflected from the SiO_2/Si interface. As expected, the amplitude of the primary pulse continually decreases during dewetting while the amplitude of the secondary pulse continually increases. As the ratio of the primary and secondary amplitudes approach unity, the destructive interference becomes more complete and the reflectivity is expected to decrease. However, close

inspection of Fig. 6(a) shows that the arrival times of both pulses are changing during dewetting.

The time delay between the arrival of the primary and secondary pulses (which is simply taken to be the time difference between the peak amplitudes of each pulse) is inset in Fig. 6(b). We see that the time delay between pulse arrivals (or phase difference) reaches a maximum for sample S5. This is a manifestation of the effective Ni layer becoming more "dielectriclike" than metallic, with respect to transmission. During the initial stages of dewetting very little SiO_2 is exposed and the majority of the transmitted radiation travels through Ni regions. Since the average height of the Ni regions is increasing, the radiation takes longer to travel to the SiO_2/Si interface, due to the slower group velocity in the Ni regions. This results in a increase in the time delay between the primary and secondary pulse. However, as the dewetting process continues the amount of exposed SiO_2 continues to increase along with the average height of the Ni regions. Between samples S4 and S5 a critical amount of exposed SiO_2 is reached, where the majority of the transmitted radiation emerges from the SiO_2/vacuum interface (this is compounded by the fact that the average height of the Ni regions is becoming thicker and transmitting less radiation). This reduces the time delay between pulses, which causes the reflectivity to increase due to the change in interference condition. Inspection of Fig. 6(b) reveals that samples S4 and S5 have identical time delays but S5 has a lower reflectivity. This is explained by noting that the ratio of amplitudes between the primary and secondary beams of S5 is closer to unity than that of S4, resulting in more complete destructive interference. Likewise, S3 and S6 have identical time delays but their differing amplitude ratios of the primary and secondary pulse produces different reflectances.

The connection between the TRDR signal and the morphology during dewetting has been more clearly elucidated from the FDTD simulations. It was found that transmission increased monotonically during dewetting, which was largely mediated by ordinary transmission through both the exposed SiO_2 and subskin depth regions of Ni. As dewetting proceeds the amount of exposed SiO_2 increases and the amount of subskin depth Ni regions decrease. This is seen as a decrease in measured reflectivity due to the more complete destructive interference as the ratio of amplitudes between the primary and secondary beams becomes closer to unity. However, as the dewetting continues a critical amount of exposed SiO_2 is reached where transmission through the effective Ni layer becomes more dielectriclike than metallic, resulting in a reduction in the time delay between the primary and secondary reflected pulses. This is seen as an increase in the measured reflectivity and the origin of the minimum observed in the TRDR signal. The minimum of the TRDR signal is expected to occur at different amounts of exposed SiO_2 for Ni films of different initial thicknesses since the transition of the effective Ni layer from metallic to dielectric is clearly dependent on the initial Ni film thickness. Moreover, the minimum of the TRDR signal during dewetting of Ni films thinner than 7.0 nm should occur at smaller amounts of exposed SiO_2 since the initial ratio of amplitudes between primary and secondary beams will be much closer to unity.

IV. DEWETTING MECHANISMS

By analyzing the sequence of AFM micrographs S1–S7 in Fig. 4 in conjunction with the TRDR data, we can more rigorously understand the mechanisms of the dewetting process. Comparing micrographs S1 and S2 we clearly observe both grain growth and a high density of grain-boundary grooves. Most grooves have a longish geometry with aspect ratios greater than unity since they extend along the planar grain-boundary/vacuum interface. As explained by Mullins,[17] grain-boundary grooving is mediated by surface diffusion and is a result of the interface evolving toward a constant curvature surface, constrained by an equilibrium dihedral angle at the grain boundary. Grain-boundary grooving has previously been observed in Ni films of comparable thickness[21] and is generally accepted as the primary mechanism of hole nucleation in solid-state dewetting.[36] Conversely, the effect of grain growth prior to the dewetting process has remained largely unexplored.

The average in-plane grain diameters of micrographs S1 and S2 are calculated using a watershed grain detection algorithm, which are found to be 14 ± 2 nm and 20 ± 2 nm, respectively. Since the initial grain size is on the order of the film thickness normal grain growth is expected to stagnate,[37] which is often attributed to the formation of grain-boundary grooves pinning the grain boundaries.[38] It must be emphasized that grain growth is not stopped but it is simply slower than normal grain growth; moreover, it has been found[39] that grain growth of ultrathin columnar films is accelerated by the surface energy driving force, which scales strongly with the inverse film thickness.[40]

The grain growth observed in AFM is further supported by the TRDR data. Inspection of the TRDR signal in Fig. 2 reveals that the reflectivity increases during the initial stages of heating (for films of initial thickness greater than 4.0 nm), which was found to be irreversible upon cooling. As previously mentioned, the optical constants of thin films are different than bulk samples due to inhomogeneities such as grain boundaries and vacancies. As seen in Fig. 3(a) the reflectivity of the 7.0 nm thick film is less than that predicted by the bulk optical constants. Therefore, an increase in grain size is consistent with the observed increase in reflectivity during the initial stages of heating since the conductivity is expected to increase with grain size[41,42] for nanoscale grains. Consequently, the optical constant of the film will approach that of the bulk values. Moreover, this effect was even detected at room temperature, as shown in Fig. 3(a) where the reflectivity is found to increase nonasymptotically after deposition.

From these data it is not necessarily clear if grain growth is the dominant mechanism responsible for the change in reflectivity. The annealing of other defects such as nonequilibrium vacancies and argon inclusions would produce similar effects.[21] However, this ambiguity is resolved by measuring the postdeposition TRDR signal of a discontinuous film at room temperature. The room temperature postdeposition measurement of reflectivity of the 2.0 nm thick film was constant found to be constant in time (within the resolution of the photodetector). This was distinctly different than all other films, which exhibited significant changes in reflectiv-

ity. It is emphasized that no detectable change in reflectivity was observed in the 2.0 nm sample, which was recorded for 2 h. Conversely, all other films showed measurable postdeposition changes in reflectivity at room temperature within the first minute and continued to change monotonically for all time scales measured (up to 13 h). From four-point probe resistance measurements, it was found that the 2.0 nm as deposited film was discontinuous while films possessing thicknesses of 3.0 m and greater were all found to be continuous. This sharp transition in the postdeposition changes in reflectivity cannot be explained by annealing of vacancies or argon inclusions since these processes will occur independent of the film continuity.[43] Therefore it can be concluded that the postdeposition change in reflectivity is a result of grain growth.

Inspection of micrograph S3 reveals large holes exposing the SiO_2, which are nucleated when the grain-boundary grooves reach the substrate. There is a wide distribution in hole size, which indicates that both hole growth and nucleation occur simultaneously. Hole growth and nucleation continues to expose greater amounts of the SiO_2 interface (micrograph S4) resulting in a further decrease in reflectivity. Eventually the percolation limit is reached (micrograph S5) where particles are connected by thin necks. Continued heating results in the necks pinching off (or particle coalescence), followed by complete breakup of the film into isolated particles (micrograph S7). After the film breakup, we see that the reflectivity continues to increase, which is a result of the isolated particles coarsening via Ostwald ripening or Smoluchowski ripening.[44]

The kinetics of these dewetting mechanisms can be analyzed *quantitatively* using the measured TRDR signal acquired during dewetting. Given that these mechanisms are thermally activated, the time τ, to reach a characteristic temperature T_0, is given by

$$\tau = A \exp\left(\frac{\Delta E}{k_b T_0}\right), \tag{4}$$

where A is a proportionality constant, ΔE is the activation energy, and k_b is the Boltzmann constant. The minimum of the TRDR curve represents a repeatable and identifiable system state with characteristic temperature T_0. Since this characteristic temperature is dependent on the applied heat rate, we can apply equation refarrhen to determine the activation energy. Using the measured $\tau - T_0$ pairs for heating rates ranging from 1.0 to 15.0 °C/min, and fitting to Eq. (4), activation energies of 0.31 ± 0.04 and 0.59 ± 0.06 eV are determined (Fig. 7). Also, nearly identical activation energies of 0.33 ± 0.04 and 0.58 ± 0.06 eV were found when applying the Kissinger-Akahira-Sunose method, which is the more common method for determining activation energies of thermally activated processes during dewetting.[4,21,45,46]

To better understand the physical origin of these activation energies we first compare the morphologies of the 4.0 and 7.5 nm thick films at the minimum of the TRDR curve. As discussed in the previous section, for films of different initial thicknesses it is expected that the minimum of the TRDR signal will occur at different stages of the dewetting process. Comparing the AFM micrographs of A1 (Fig. 8) to

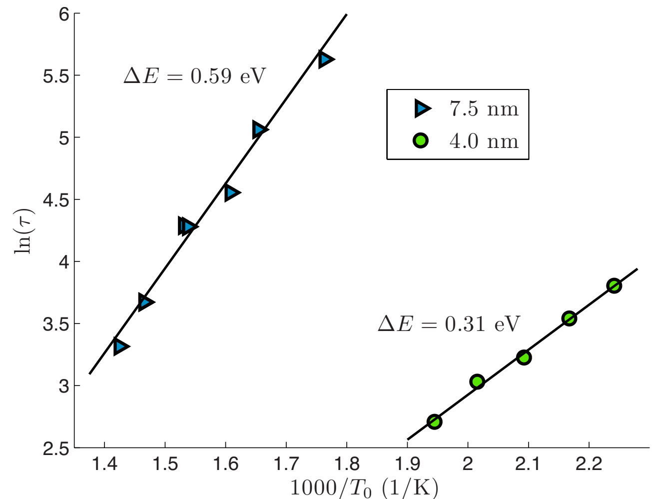

FIG. 7. (Color online) Arrhenius plots for the thermally activated processes characterized by the temperature T_0 corresponding to the minimum of the TRDR curve. Films of 4.0 and 7.5 nm thickness are used, and heating rates range from 1.0 to 15.0 °C/min.

S5 (Fig. 4) we see that this is indeed the case, as the morphologies are significantly different. A1 is in the early stages of dewetting where grain growth and grain-boundary grooving are the prominent mechanisms of morphological evolution. Grain-boundary grooving is unlikely to be the rate-limiting step, as the we would expect the activation barrier to be at least high as that found for surface mass diffusion along the low index planes of Ni. Ondrejcek *et al.*[47] have measured an activation barrier of 0.65 eV for surface mass diffusion on the (111) planes of Ni while Bonzel and Latta[48] found a value of 0.76 eV on the (110) planes. This strongly suggests that the measured activation energy of 0.31 eV corresponds to the rate-limiting process during grain growth in 4.0 nm thick Ni films on SiO_2 at temperatures of ~500 K.

By direct measurement of grain size in scanning electron microscopy, an activation energy of 0.25 eV was measured during annealing of Ni thin films.[49] The 4.0 nm thick Ni films were deposited using e-beam evaporation onto a mica substrate, and were annealed at temperatures ranging from 90 to 420 °C. This agrees well with our measured value of 0.31 eV, where the 0.06 eV difference is possibly due to the different substrate and deposition method used in this study. Also, as already discussed in significant detail, both the TRDR and AFM data strongly suggest that grain growth occurs during the initial stages of dewetting. We therefore propose that the measured activation energy of 0.31 eV corresponds to the rate-limiting mechanism of Ni grain growth at ~500 K. Other reports on grain growth in fcc metal films performed at these temperatures also find similar activation energies.

From TEM measurements of grain size, the measured activation energy during grain growth in Au thin films was found to be 0.14 eV,[50] 0.36 eV for thin films of Cu,[51] and 0.274 eV for thin films of Ag.[52] These reported activation barriers for grain growth are typically attributed to the additional driving force provided by interface[53] and surface energy minimization[40] for thin films. It has also been suggested

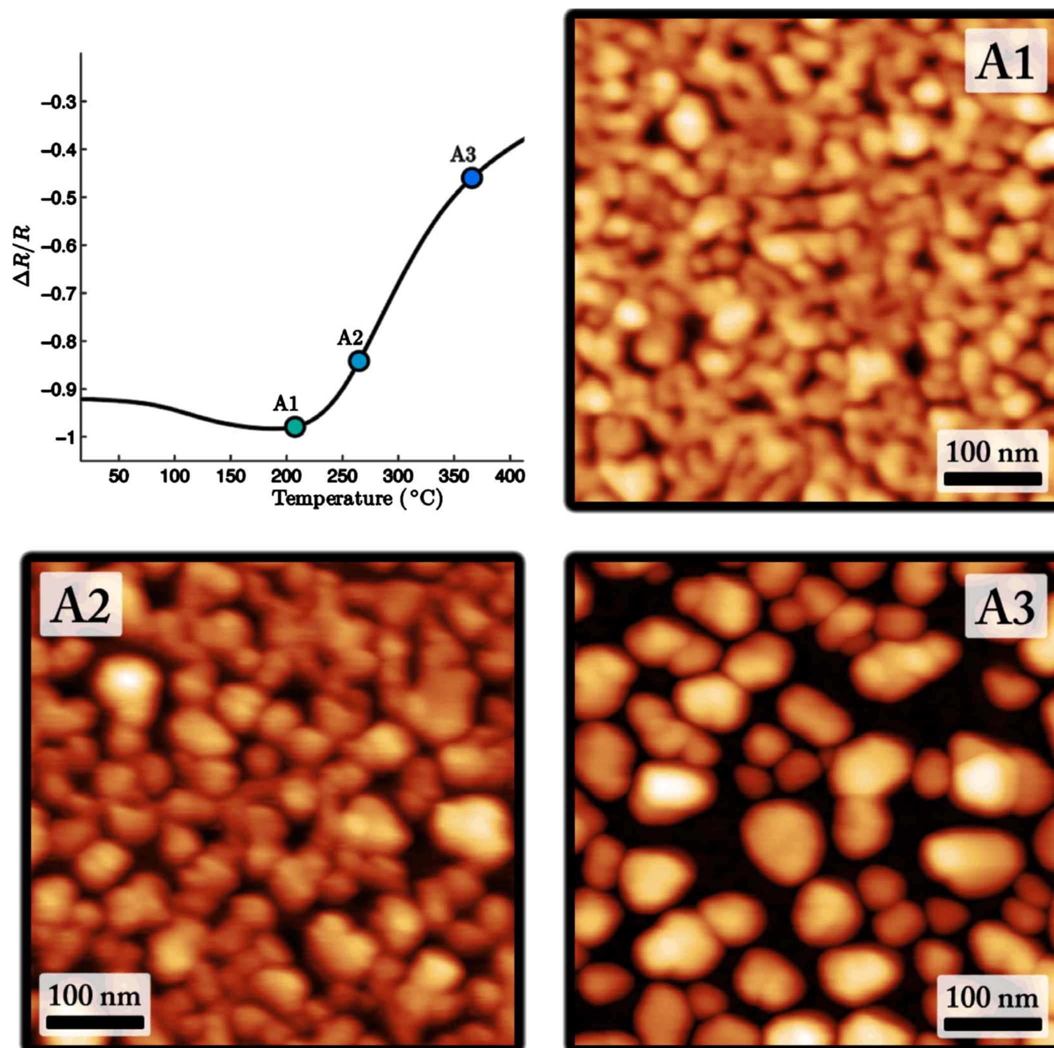

FIG. 8. (Color online) *Ex situ* AFM micrographs of a 4.0 nm thick Ni films during different stages of dewetting. The corresponding positions on the TRDR curve are shown.

that the high density of defects, such as dislocations and twins contribute significantly to the driving force.[51,54]

Next we turn our attention to the measured activation energy of 0.59 ± 0.06 eV. Inspection of micrographs S3–S5 (Fig. 4) reveals that hole growth is the dominant mechanism of film breakup during this stage of dewetting. During hole growth the film locally thins via retraction of the hole edge, consequently there must be local film thickening within the interior region of the film. This suggests that the activation energy of 0.59 eV corresponds to either the rate-limiting process during local film thinning, mass transport across the Ni surface, or local film thickening.

The local thickening effect can be seen in micrographs S3–S5, where large faceted particles are observed. It is also found that the number of faceted particles increases as dewetting proceeds, as does the average particle size and height. Using KMC simulations, Combe *et al.*[55] have investigated the mechanism of shape change for isolated, defectfree, and faceted nanoparticles. It was found that the rate-limiting step to particle relaxation was the nucleation of two-dimensional (2D) islands on the facets. As estimated by Mullins and Rohrer,[56] the nucleation rate of 2D islands is negligible for particles $\gtrsim 1.0$ nm. This extremely large nucleation barrier has also been confirmed by other authors,[57,58] where the nucleation barrier is generally found to be proportional to the particle size.

However, recent investigations into faceted nanoparticle agglomeration have revealed a much richer and complex behavior than single-particle shape change.[59–61] In these studies, it has been found that the coalescence rate is strongly influenced by the particle orientation. Specifically, McCarthy and Brown have shown that 2D nucleation is not required for a pair of coalescing fcc particles intersecting at the (111) plane. This is because step-flow growth of the (111) layers is possible on these favorably oriented particles, making a continuous stepped morphology across the neck region. Moreover, the activation barrier to coalescence was found to be independent of size for (111) oriented particles and the rate-limiting step was due to surface mass diffusion.

Despite the idealized scenario of faceted particle coalescence, we expect the mechanism of local film thickening during latter stages of dewetting to occur in a similar manner.

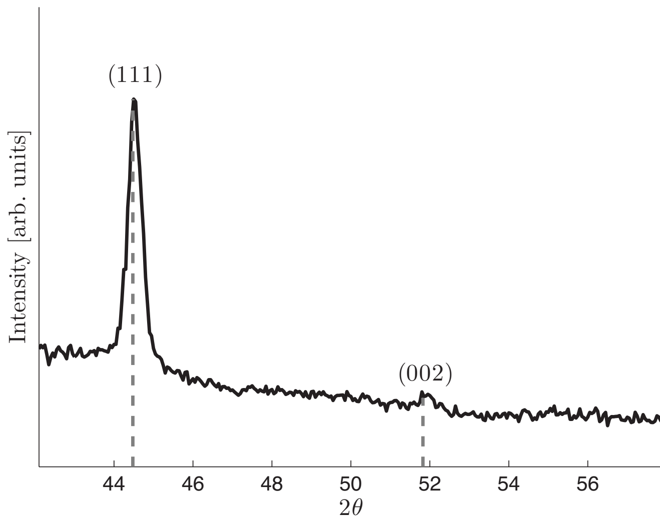

FIG. 9. XRD scan of 7.5 nm thick Ni film during dewetting (sample S4, see Fig. 4). This shows that the Ni films are heavily (111) textured during this stage of dewetting.

Specifically, local thickening proceeds by surface diffusion on the Ni surface, where favorably oriented faceted grains are able to coalesce via a heterogeneous nucleation mechanism. In this scenario, the rate-limiting step is surface diffusion along the planes of favorably oriented coalescing grains. From XRD data (Fig. 9) we see that the Ni films are strongly (111) oriented during dewetting. This strong (111) texture is a result of preferential orientation during deposition[62] and grain reconfiguration during annealing.[63] Therefore, we expect that the local thickening of the Ni films during dewetting is limited by surface diffusion along the (111) planes.

Likewise, Ni surface diffusion is also expected to be the mechanism of local film thinning. Inspections of micrographs S3–S5 shows that most holes in the film are not completely bounded by facets. Therefore, the classical mechanism of hole-edge retraction is expected to be valid in these regions.[36] Due to the larger curvature at the hole boundary, the driving force for local film thinning is provided by curvature induced surface diffusion.

Therefore, we find that the processes of local film thickening, mass transport across the Ni surface, and local film thinning are all limited by surface self-diffusion along the Ni(111) planes. Recently, the activation energy for surface mass self-diffusion on the Ni(111) surface was measured to be 0.65 ± 0.1 eV,[47] which agrees very well with our measured activation energy of 0.59 ± 0.06 eV. In light of the above discussion, this strongly suggests that the rate-limiting step during the later stages of dewetting Ni is surface self-diffusion along the (111) planes.

From the kinetic analysis we have measured activation energies of 0.31 ± 0.04 and 0.59 ± 0.06 eV, which are found to correspond to grain growth and hole growth via surface mass self-diffusion along the Ni(111) planes. It should be noted that these activation energies were measured from films of different thicknesses. Looking at the sequential dewetting AFM micrographs of both the 7.0 nm film (Fig. 4) and the 4.0 nm film (Fig. 8) the processes of grain growth and hole growth can both be clearly identified. It is therefore expected that both of these processes will occur as rate-limiting steps in this thickness regime. However, at higher film thicknesses, a (001) texture can often be found in fcc metal films.[40] This may significantly impact the process of hole growth, due to the importance of grain orientation on the local thickening film. Likewise, at extremely small thicknesses, the density of grain-boundary grooves may be sufficiently high such that Ni surface diffusion on the SiO_2 substrate becomes rate-limiting during hole growth. Further investigation is required to understand what the rate-limiting mechanisms are outside of the studied thickness regime.

V. CONCLUSIONS

We studied the dewetting of 2.0–9.0 nm thick Ni thin films on amorphous SiO_2 using TRDR, which is a real-time technique and was performed *in situ*. This was combined with *ex situ* AFM. FDTD simulations, which used the experimentally acquired AFM heightmaps as inputs, were used to better understand the observed TDRD signal and its connection to morphological changes during dewetting. FDTD simulations revealed a monotonic increase in transmission during the dewetting process and the existence of hole/particle site resonances. The site resonances become increasingly intense with wavelength, resulting in weak extraordinary transmission in some cases. However, it was found that transmission is dominated by ordinary transmission through the SiO_2 and subskin depth regions of Ni, and the scattering from the Ni particles/holes. Furthermore, FDTD simulation revealed that the observed minimum of the TRDR signal during dewetting is a consequence of a transmission through the effective Ni layer becoming more dielectriclike than metallic. During this transition the ratio of amplitudes between the primary and secondary pulses approach unity while the trend in time delay between pulses reverses. This extremum in time delay between pulses is the origin of the minimum observed in the TRDR signal.

Analysis of the *ex situ* AFM micrographs revealed the sequential processes of grain growth, grain-boundary grooving, hole growth, and particle coarsening. The presence of grain growth was further substantiated by the TRDR data; after deposition, all continuous films (≥ 3.0 nm) exhibited a nonasymptotic monotonic change in reflectivity. Conversely, the discontinuous 2.0 nm film did not show any detectable changes in reflectivity postdeposition. The dewetting literature has typically neglected grain growth in ultrathin films prior to hole nucleation. However, grain growth is particularly important since the final particle density is critically determined by the initial grain-boundary density.

Lastly, the TRDR data was used to identify two kinetic pathways during dewetting of Ni on SiO_2. These kinetic pathways were found to have activation energies of 0.31 ± 0.04 and 0.59 ± 0.06 eV. From these data we proposed that the physical origin of these activation energies are a result of Ni grain growth and surface mass self-diffusion on Ni(111), respectively.

ACKNOWLEDGMENTS

The authors would also like to thank Timo Ewalds for his

expert help on coding KMC simulations of dewetting and Peter Kalisvaart for his detailed revision of the manuscript. This study was funded by the Natural Sciences and Engineering Research Council of Canada and Alberta Ingenuity.

[1] C. Boragno, F. Buatier de Mongeot, R. Felici, and I. K. Robinson, Phys. Rev. B **79**, 155443 (2009).
[2] K. Thürmer, E. D. Williams, and J. E. Reutt-Robey, Phys. Rev. B **68**, 155423 (2003).
[3] B. Yang P. Zhang, D. E. Savage, M. G. Lagally, G.-H. Lu, M. Huang, and F. Liu, Phys. Rev. B **72**, 235413 (2005).
[4] R. Saxena, M. J. Frederick, G. Ramanath, W. N. Gill, and J. L. Plawsky, Phys. Rev. B **72**, 115425 (2005).
[5] Y. J. Oh, C. A. Ross, Y. S. Jung, Y. Wang, and C. V. Thompson, Small **5**, 860 (2009).
[6] D. Kim, A. L. Giermann, and C. V. Thompson, Appl. Phys. Lett. **95**, 251903 (2009).
[7] F. Fillot, Z. Tőkei, and G. P. Beyer, Surf. Sci. **601**, 986 (2007).
[8] I. Lazić, P. Klaver, and B. Thijsse, Phys. Rev. B **81**, 045410 (2010).
[9] A. Hashibon, A. Y. Lozovoi, Y. Mishin, C. Elsässer, and P. Gumbsch, Phys. Rev. B **77**, 094131 (2008).
[10] S. H. Lim, D. Derkacs, and E. T. Yu, J. Appl. Phys. **105**, 073101 (2009).
[11] M. A. Seo *et al.*, Nat. Photonics **3**, 152 (2009).
[12] G. D. Nessim, A. J. Hart, J. S. Kim, D. Acquaviva, J. Oh, C. D. Morgan, M. Seita, J. S. Leib, and C. V. Thompson, Nano Lett. **8**, 3587 (2008).
[13] G. D. Nessim M. Seita, K. P. OBrien, A. J. Hart, R. K. Bonaparte, R. R. Mitchell, and C. V. Thompson, Nano Lett. **9**, 3398 (2009).
[14] L. Rayleigh, Proc. London Math. Soc. **10**, 4 (1878).
[15] M. E. T. Molares, A. G. Balogh, T. W. Cornelius, R. Neumann, and C. Trautmann, Appl. Phys. Lett. **85**, 5337 (2004).
[16] A. E. B. Presland, G. L. Price, and D. L. Trimm, Surf. Sci. **29**, 435 (1972).
[17] W. W. Mullins, J. Appl. Phys. **28**, 333 (1957).
[18] D. J. Srolovitz and S. A. Safran, J. Appl. Phys. **60**, 247 (1986).
[19] J. J. Rha and J. K. Park, J. Appl. Phys. **82**, 1608 (1997).
[20] O. Pierre-Louis, A. Chame, and Y. Saito, Phys. Rev. Lett. **103**, 195501 (2009).
[21] J. Petersen and S. G. Mayr, J. Appl. Phys. **103**, 023520 (2008).
[22] R. Felici, N. M. Jeutter, V. Mussi, F. B. de Mongeot, C. Boragno, U. Valbusa, A. Toma, Y. W. Zhang, C. Rau, and I. K. Robinson, Surf. Sci. **601**, 4526 (2007).
[23] R. Lazzari, G. Renaud, C. Revenant, J. Jupille, and Y. Borensztein, Phys. Rev. B **79**, 125428 (2009).
[24] J. Dufourcq, P. Mur, M. J. Gordon, S. Minoret, R. Coppard, and T. Baron, Mater. Sci. Eng., C **27**, 1496 (2007).
[25] A. Romo-Negreira, D. J. Cott, S. De Gendt, K. Maex, M. M. Heyns, and P. M. Vereecken, J. Electrochem. Soc. **157**, K47 (2010).
[26] Y. T. Jeon, J. Y. Moon, G. H. Lee, J. Park, and Y. Chang, J. Phys. Chem. B **110**, 1187 (2006).
[27] H. Qiu, G. Safran, B. Pecz, P. B. Barna, A. Kosuge, H. Nakai, S. Yugo, and M. Hashimoto, Thin Solid Films **229**, 107 (1993).
[28] S. Larouche and L. Martinu, Appl. Opt. **47**, C219 (2008).
[29] D. E. Aspnes, Thin Solid Films **89**, 249 (1982).
[30] M. Gilliot, A. En Naciri, L. Johann, J. P. Stoquert, J. J. Grob, and D. Muller, Phys. Rev. B **76**, 045424 (2007).
[31] R. Lazzari and I. Simonsen, Thin Solid Films **419**, 124 (2002).
[32] K. L. van der Molen, K. J. Klein Koerkamp, S. Enoch, F. B. Segerink, N. F. van Hulst, and L. Kuipers, Phys. Rev. B **72**, 045421 (2005).
[33] F. J. García de Abajo, J. J. Sáenz, I. Campillo, and J. S. Dolado, Opt. Express **14**, 7 (2006).
[34] T. Matsui, A. Agrawal, A. Nahata, and Z. V. Vardeny, Nature (London) **446**, 517 (2007).
[35] M. Born and E. Wolf, *Principles of Optics*, 7th ed. (Cambridge University Press, Cambridge, 1999).
[36] E. Jiran and C. V. Thompson, Thin Solid Films **208**, 23 (1992).
[37] C. V. Thompson, Annu. Rev. Mater. Sci. **20**, 245 (1990).
[38] W. W. Mullins, Acta Metall. **6**, 414 (1958).
[39] R. A. Ristau, K. Barmak, K. R. Coffey, and J. K. Howard, J. Mater. Res. **14**, 3263 (1999).
[40] C. V. Thompson, Interface Sci. **6**, 85 (1998).
[41] J. M. Camacho and A. I. Oliva, Thin Solid Films **515**, 1881 (2006).
[42] A. F. Mayadas and M. Shatzkes, Phys. Rev. B **1**, 1382 (1970).
[43] Z. Zhou and B. Jóos, Surf. Sci. **323**, 311 (1995).
[44] P. A. Thiel, M. Shen, D. J. Liu, and J. W. Evans, J. Phys. Chem. C **113**, 5047 (2009).
[45] M. J. Starink, Thermochim. Acta **404**, 163 (2003).
[46] M. J. Frederick, R. Goswami, and G. Ramanath, J. Appl. Phys. **93**, 5966 (2003).
[47] M. Ondrejcek, M. Rajappan, W. Swiech, and C. P. Flynn, Phys. Rev. B **73**, 035418 (2006).
[48] H. P. Bonzel and E. E. Latta, Surf. Sci. **76**, 275 (1978).
[49] V. Starý and K. Šefčik, Vacuum **31**, 345 (1981).
[50] N. Mancini and E. Rimini, Surf. Sci. **22**, 357 (1970).
[51] S. Simões, R. Calinas, M. T. Vieira, M. F. Vieira, and P. J. Ferreira, Nanotechnology **21**, 145701 (2010).
[52] R. Dannenberg, E. A. Stach, J. R. Groza, and B. J. Dresser, Thin Solid Films **370**, 54 (2000).
[53] E. A. Holm and S. M. Foiles, Science **328**, 1138 (2010).
[54] C. Detavernier, S. Rossnagel, C. Noyan, S. Guha, C. Cabral, Jr., and C. Lavoie, J. Appl. Phys. **94**, 2874 (2003).
[55] N. Combe, P. Jensen, and A. Pimpinelli, Phys. Rev. Lett. **85**, 110 (2000).
[56] W. W. Mullins and G. R. Rhorer, J. Am. Ceram. Soc. **83**, 214 (2000).
[57] A. La Magna, Surf. Sci. **601**, 308 (2007).
[58] K. Thürmer and N. C. Bartelt, Phys. Rev. Lett. **100**, 186101 (2008).
[59] J. Rankin and B. W. Sheldon, J. Am. Ceram. Soc. **82**, 1868 (1999).
[60] L. J. Lewis, P. Jensen, and J. L. Barrat, Phys. Rev. B **56**, 2248 (1997).
[61] D. N. McCarthy and S. A. Brown, Phys. Rev. B **80**, 064107 (2009).
[62] Y. Golan, L. Margulis, and I. Rubinstein, Surf. Sci. **264**, 312 (1992).
[63] M. J. Rost, D. A. Quist, and J. W. M. Frenken, Phys. Rev. Lett. **91**, 026101 (2003).